

This is the accepted manuscript made available via CHORUS. The article has been published as:

Pyrochlore electrons under pressure, heat, and field: Shedding light on the iridates

William Witczak-Krempa, Ara Go, and Yong Baek Kim

Phys. Rev. B **87**, 155101 — Published 1 April 2013

DOI: [10.1103/PhysRevB.87.155101](https://doi.org/10.1103/PhysRevB.87.155101)

Pyrochlore electrons under pressure, heat and field: shedding light on the iridates

William Witczak-Krempa¹, Ara Go², Yong Baek Kim^{1,3}

¹*Department of Physics, University of Toronto, Toronto, Ontario M5S 1A7, Canada*

²*Department of Physics, Columbia University, New York, New York 10027, USA*

³*School of Physics, Korea Institute for Advanced Study, Seoul 130-722, Korea*

(Dated: March 12, 2013)

We study the finite temperature and magnetic field phase diagram of electrons on the pyrochlore lattice subject to a local repulsion as a model for the pyrochlore iridates. We provide the most general symmetry-allowed Hamiltonian, including next-nearest neighbour hopping, and relate it to a Slater-Koster based Hamiltonian for the iridates. It captures Lifshitz and/or thermal transitions between several phases such as metals, semimetals, topological insulators and Weyl semimetals, and gapped antiferromagnets with different orders. Our results on the charge conductivity, both DC and optical, Hall coefficient, magnetization and susceptibility show good agreement with recent experiments and provide new predictions. As such, our effective model sheds light on the pyrochlore iridates in a unified way.

I. INTRODUCTION

The pyrochlore iridates, $R_2\text{Ir}_2\text{O}_7$ (R-227) where R is a rare earth, provide an ideal setup to study the interplay of correlations, band topology and frustration. Building in part on the strong role of spin-orbit coupling (SOC) and correlations for Ir,¹ various novel phases have been predicted to potentially occur in this family of complex oxides such as fractionalized topological insulators^{2,3} (TIs), chiral spin liquids,⁴ topological Weyl semimetals^{5,6} (TWSs), and axion insulators.^{5,7} This has contributed to a substantial experimental effort,^{8–21} in particular to determine the nature of the still-elusive magnetic ordering, except for Pr-227 which shows no sign of long-range order down to the lowest accessible temperatures. Recent theoretical and experimental work has been pointing towards a $q = 0$ all-in/all-out (AIO) magnetic pattern in the ground state^{5,6,14–16,20,21} but direct evidence is still lacking. Another question concerns the nature of the metal insulator transition as a function of chemical pressure via the change of the R-site element^{8,11,12} or hydrostatic pressure,^{17,18} as well as the nature of the thermal continuous transitions: what are the respective roles of magnetic ordering, Mott physics, and band structure? Finally, are any of the new phases, for example the TWS, present in the actual compounds?

We provide insight into these questions by considering a microscopically-motivated Hubbard model which we probe at finite temperature and magnetic field. We compute transport, magnetization and susceptibility in the various phases (metal (M), TI, TWS, AIO, antiferromagnet (AF), etc) as well as their behaviour across the phase transitions, quantum or thermal. The similarity of our results with recent experimental data allows us to make guesses on the locations of different iridates in our phase diagram, and make predictions for future experiments. Before considering the observables, we discuss a fully general Hubbard Hamiltonian on the pyrochlore lattice, its relation to previous models used for the iridates, and to the new model underlying this work.

The iridium ions form a pyrochlore lattice of corner-

sharing tetrahedra and have a partially filled shell of 5d electrons. This results in the local repulsion and spin orbit coupling being of similar size, both on the order of 0.5-1 eV.^{2,5} The localized f-electrons of the R-site (absent for Y) can complicate the picture for some members of the iridates family for which the R-site ion carries a net magnetic moment. In this work we shall not consider the interplay between these local moments and the more itinerant Ir d-electrons. As such, our results apply directly to the compounds with Y, Lu and Eu for which this complication does not arise. Regarding the compounds with a magnetic R-site, such as for $R = \text{Nd}, \text{Sm}, \text{Yb}$, etc, the Ir d-electron physics might still play a key role. Indeed, the similarity of the phenomena across the pyrochlore iridates family, independent of whether the R-site is magnetic or not, provide weight to this statement.^{8,9,11–13,21} In the context of the pyrochlore iridates, a recent work²² has examined the interplay between the more itinerant d-electrons and the localized f-electron moments by including an exchange coupling between our nearest neighbor hopping Hamiltonian,⁶ Eq. (1), and an appropriate spin model. It was found that Weyl semimetal and axion insulator^{5,7} phases can be induced by the $f-d$ exchange, and that the latter can cooperate with the Hubbard interaction on Ir sites to stabilize the Weyl semimetal over a larger region of parameter space than when it is induced by d-electron correlations alone. Further studies in that direction will be of interest, notably to get a better understanding of the chiral spin liquid behavior of Pr-227.⁴

The outline is as follows: we first introduce the general Hamiltonian in Section II and relate it to previous works. The ground state phase diagram and its extension to finite temperature is obtained in Section III. The conductivities, both d.c. and optical, are then discussed in Section IV. We discuss the finite-magnetic field phase diagram in Section V. Finally, we briefly summarize in Section VI and draw connections between our results and experiments on the pyrochlore iridates.

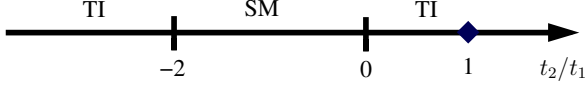


FIG. 1. Phase diagram of the generic NN hopping Hamiltonian on a pyrochlore lattice. It has two possible phases: a TI and a SM. The square indicates the presence of a gap closing, surrounded by the TI phase.

II. MODEL DEMYSTIFIED

Rather than starting with a specific microscopic model for the iridates, we consider the most generic, time-reversal invariant Hubbard Hamiltonian on the pyrochlore lattice. We shall focus on an effective model with a single Kramers' doublet at each Ir site. This will lead to an 8-band model that we believe is sufficient to capture the salient physics. We write the Hamiltonian in a *global* basis for the pseudospin to emphasize its simplicity and generality:

$$H_0 = \sum_{\langle i,j \rangle} c_i^\dagger (t_1 + it_2 \mathbf{d}_{ij} \cdot \boldsymbol{\sigma}) c_j + \sum_{\langle\langle i,j \rangle\rangle} c_i^\dagger (t'_1 + i[t'_2 \mathbf{R}_{ij} + t'_3 \mathbf{D}_{ij}] \cdot \boldsymbol{\sigma}) c_j, \quad (1)$$

where $\boldsymbol{\sigma}$ is a vector of Pauli matrices acting on the pseudospin degree of freedom, which in the context of the iridates can be thought of as arising from the splitting of the t_{2g} levels by SOC¹ and/or trigonal distortions^{23,24} and subsequent projection onto a half-filled doublet near the Fermi level (E_F). The real vectors \mathbf{d}_{ij} , \mathbf{R}_{ij} , \mathbf{D}_{ij} depend on the given bond as follows: \mathbf{d}_{ij} is aligned along the opposite bond of the tetrahedron containing i, j (Fig. 8(a)); it is parallel or antiparallel with the nearest neighbor (NN) Dzyaloshinski-Morya (DM) vector of a spin model on the pyrochlore lattice, of which there are only two symmetry-allowed configurations,^{6,25} differing by a global sign. \mathbf{R}_{ij} , \mathbf{D}_{ij} are obtained by going to the next nearest neighbour (NNN) via the common NN site and taking a cross product of the two bond or \mathbf{d}_{ij} vectors encountered, respectively. See Appendix A for details regarding the construction of Eq. (1). The five real hopping amplitudes lead to a four-parameter free model, to which we add a Hubbard repulsion term, $H_U = (U/2) \sum_i (n_i - 1)^2$. In this work we perform a mean field decoupling of H_U in the magnetic channel, but expect many results to survive the inclusion of quantum many-body effects. Indeed, a subset of many-body effects was taken into account in our recent study⁷ of the NN Hamiltonian using cellular dynamical mean-field theory (CDMFT). For instance, we obtained the same magnetic orders as those found at the mean-field field level.

Before discussing the relation of Eq. (1) to previous microscopic models for the iridates and to the one used

in this work, we briefly discuss the phase diagram including only NN hopping. It depends on a single parameter, t_2/t_1 , and can be determined exactly at half-filling; the result is shown in Fig. 1. For $-2 < t_2/t_1 < 0$ a semimetal (SM) results, and otherwise we have a TI,²⁶ with the exception of $t_2/t_1 = 1$ where an accidental gap closing occurs. Interestingly, it does not alter the topological structure of the Hamiltonian such that the TI survives to arbitrary large values of t_2/t_1 . The SM is characterized by lines of nodes between the Γ and L points. The phase transitions at $t_2/t_1 = -2, 0$ occur via gap closing/opening at the Γ point. At $t_2 = 0$, the Hamiltonian can be diagonalized analytically.²⁷ Interestingly, it is also the case at $t_2/t_1 = -2$, where the band structure corresponds exactly to the $t_2 = 0$ case, albeit with a spectrum inversion; specifically: $\{t_1 = 1, t_2 = -2\}$ maps to $\{-3, 0\}$. The phase transition at $t_2/t_1 = 0$ was previously discussed,²⁸ where the $t_{1,2}$ model was identified as the most general NN symmetry-allowed Hamiltonian.

We now relate the general parameters to microscopically-motivated ones for the iridates. We first consider the case of no trigonal distortion,^{2,6} leading to ideal oxygen octahedra surrounding the iridiums. The SOC splits the t_{2g} manifold into $J_{\text{eff}} = 1/2$ and $3/2$ multiplets. Projecting onto the half-filled doublet near E_F yields a pseudospin $J_{\text{eff}} = 1/2$ description. Going from the atomic picture to the lattice, we introduce oxygen-mediated² and direct⁶ overlap NN hopping t_{oxy} and t_σ, t_π , respectively. These relate to the generic model hoppings via:

$$\begin{aligned} t_1 &= \frac{130t_{\text{oxy}}}{243} + \frac{17t_\sigma}{324} - \frac{79t_\pi}{243}; & t'_1 &= \frac{233t'_\sigma}{2916} - \frac{407t'_\pi}{2187}; \\ t_2 &= \frac{28t_{\text{oxy}}}{243} + \frac{15t_\sigma}{243} - \frac{40t_\pi}{243}; & t'_2 &= \frac{t'_\sigma}{1458} + \frac{220t'_\pi}{2187}; \\ t'_3 &= \frac{25t'_\sigma}{1458} + \frac{460t'_\pi}{2187}; \end{aligned} \quad (2)$$

where we have also added $t'_{\sigma,\pi}$, the σ - and π -overlap NNN hoppings. We see that the microscopic model already saturates the general Hamiltonian. As such, small trigonal distortions²³ will renormalize the t'_a but will not contribute new terms allowing us to use the $J_{\text{eff}} = 1/2$ description without loss of generality. We mention that Ref. 2 used purely oxygen mediated hopping, hence their large SOC TI can be mapped to $t_2/t_1 = 14/65 \approx 0.215$ which indeed corresponds to a TI in Fig. 1. Also, Ref. 27 studied TIs in the t_1, t'_2 model.

We shall work in units of t_{oxy} in the rest of the paper. As before, we choose a representative subset of direct hoppings, $t_\pi = -2t_\sigma/3$, which translates to $t_1 = 0.53 + 0.27t_\sigma$ and $t_2 = 0.12 + 0.17t_\sigma$. We plot the relation between t_2/t_1 and t_σ/t_{oxy} in Fig. 9. An important addition in this work is the presence of small NNN hoppings: $t'_\sigma/t_\sigma = t'_\pi/t_\pi = 0.08$. These are expected to appear in the effective pseudospin model, and will remove line Fermi surfaces at E_F in some portions of the phase diagram, giving instead a TWS or metal with small

pockets.⁶ The line nodes are an artifact of the NN band structure.

III. PHASE DIAGRAM

The mean field phase diagram is shown in Fig. 2. At $T = 0$ and small U , it contains metallic (M), SM and TI phases depending on t_σ . The metallic state has electron- and hole-like pockets while the SM is associated with a quadratic band touching, that splits into 8 linearly dispersing touchings in the AF TWS,⁶ see the spectra in Fig. 3(b) or in Fig. 5 c). The shaded regions break TRS due to the appearance of either the symmetric AIO order (pale blue), or orders which are related to the AIO state by local $\pi/2$ rotations⁶ (denoted by AIO', in green). At intermediate U , there is an extended region of TWS, which turns into a metallic AF (mAF) for $t_\sigma < -1.085$. The latter is actually a tilted TWS, where the 3D “Dirac cones” have been tilted such as to create metallic pockets, but with the “Weyl touchings” remaining, see Fig. 3(a). These phases should be compared with similar results obtained in Ref.⁶ by two of us. The main difference is that we have now included the NNN hoppings in the self-consistent treatment. Indeed, the previous work was mainly concerned with the self-consistent analysis of the NN Hamiltonian: the NNN hoppings were added to the final spectrum to establish that the line-nodes at E_F can give rise to a Weyl phase when the ordering is of the AIO type. The present work confirms this. Moreover, a metallic phase now appears for $t_\sigma < -1.085$, which will be relevant when we compare with experiments on the iridates. Another new feature is the presence of magnetization “jumps” that appear within the AIO phase, present for $-0.78 < t_\sigma < -0.68$, denoted by the orange (larger) markers in Fig. 2. The spontaneous onsite magnetization, m , grows abruptly along that line and the TWS becomes a gapped AF insulator: energetically, the system finds it preferable to preempt the continuous annihilation of Weyl points of opposite chirality via a discontinuous evolution of m , this is illustrated in Fig. 4. The abrupt continuous increase of magnetization seems tied to the peculiar spectrum of the TWS.

Turning to finite temperature, we find that most thermal transitions are continuous; this is denoted by the out-of-plane fibers ended by circular markers in Fig. 2. We have also examined the model at larger NNN hoppings, $t'_{\sigma,\pi}/t_{\sigma,\pi} = 0.16$, and found that small regions of 1st order transitions to the AIO phase appear at intermediate U . As can be seen in Fig. 2, the transition temperatures naturally increase with U , since an increase in the latter leads to larger gaps. Thus, *the gapless TWS is fairly unstable to melting at finite T* , with typical transition temperatures $T_c \sim 0.01$ in units of t_{oxy} . We note that the continuous transitions are consistent with experimental data on the pyrochlore iridates.

IV. CONDUCTIVITIES

A. Optical conductivity

We examine the optical conductivity associated with the various phases, as illustrated in Fig. 5. Panel a) shows the Lifshitz transition associated with a change in the Fermi surface topology from a metal with small electron- and hole-like pockets at $U = 0$ to a gapped AIO state at $U = 1$. The optical conductivity in panel b) reflects this via a small Drude peak in the former case, and a gap in the latter. Panel c) shows the spectra of the TWS and quadratic band touching SM out of which it arose. The associated conductivities are reduced approaching the DC limit because these two states have a vanishing density of states (DOS) at E_F . We note the distinguishing peak at low frequency for the TWS: it receives weight from transitions across the depleted energy range corresponding to the TWS, where the DOS vanishes quadratically.

B. DC transport

We turn to the DC electric transport, which provides further insight into the phase diagram. The AIO state has isotropic conductivities due to the highly symmetric magnetic configuration, i.e. $\sigma_{xx} = \sigma_{yy} = \sigma_{zz}$. The same holds for the Hall conductivities: $\sigma_{xy} = \sigma_{yz} = \sigma_{zx}$. This will cease to be true for the AIO' states, which select a given direction.⁶ To compute the transport coefficients in the DC limit, we introduce a momentum independent scattering time, τ . For example, the longitudinal and Hall conductivities are given by^{29,30}

$$\begin{aligned}\sigma_{xx} &= e^2 \tau \frac{1}{V} \sum_{\mathbf{k}, \alpha} \left(-\frac{\partial n_F}{\partial \epsilon_\alpha(\mathbf{k})} \right) (v_x^\alpha(\mathbf{k}))^2, \\ \sigma_{xy} &= e^3 \tau^2 B_z \frac{1}{V} \sum_{\mathbf{k}, \alpha} \left(\frac{\partial n_F}{\partial \epsilon_\alpha(\mathbf{k})} \right) v_y^\alpha (v_x^\alpha \partial_y - v_y^\alpha \partial_x) v_x^\alpha,\end{aligned}\tag{3}$$

where $1 \leq \alpha \leq 8$ is the index associated with the energy band ϵ_α , the corresponding band velocity is $\mathbf{v}^\alpha = \partial_{\mathbf{k}} \epsilon_\alpha$. In the Hall conductivity σ_{xy} , B_z is the component of the magnetic field in the z -direction. Fig. 6 shows the longitudinal resistivity, ρ_{xx} , and Hall coefficient, R_H , at $t_\sigma = -1.2$ and $U = 1.25$ as a function of temperature. At large temperatures, the system is in a paramagnetic metallic state, with the expected $d\rho_{xx}/dT > 0$. As T is lowered beneath $T_c = 0.21$, the system undergoes a continuous transition to the AIO AF: the on-site magnetization increases resulting in the spectrum evolving from being gapless at T just below T_c , to a fully gapped AF at the lowest temperatures. We indeed find that the resistivity shows a rapid upturn at T_c (where the slope changes sign) and becomes exponentially activated at low T . The Hall

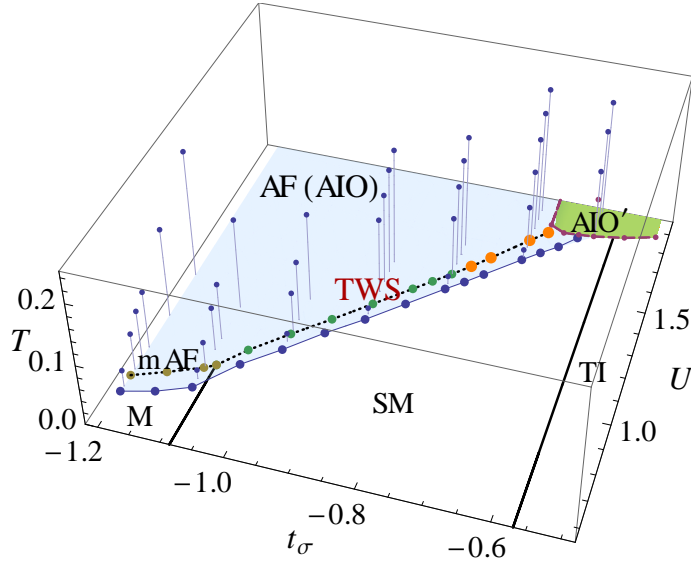


FIG. 2. Finite U & T mean field phase diagram, including small NNN hopping ($t_{\text{oxy}} = 1$). The out-of-plane fibers give T_c for the continuous transition at which the magnetic order melts. The two shaded regions correspond to AF phases: either the AIO AF, or a type related by $\pi/2$ rotations, AIO'. The solid/dashed lines denote 2nd/1st order quantum phase transitions, while the dotted lines in the AIO phase, a gap closing signaling a Lifshitz transition out of the TWS or metallic AF (mAF).

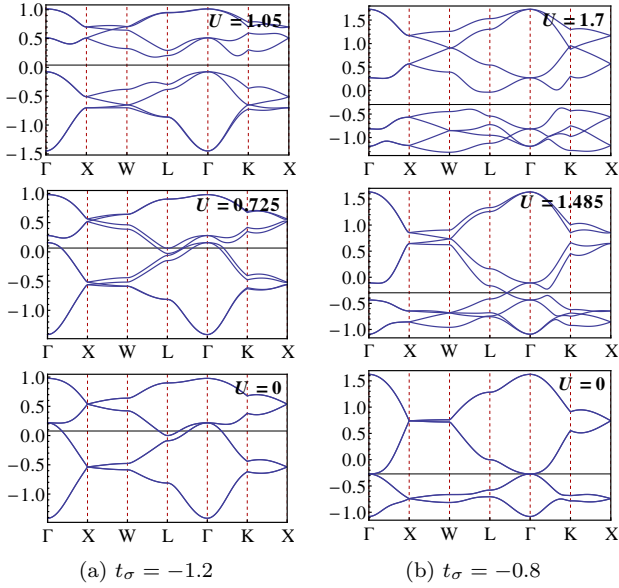


FIG. 3. Spectra for the Hamiltonian Eq. (1) for (a) $t_\sigma = -1.2$ and (b) $t_\sigma = -0.8$. These are associated with the phase diagram Fig. 2.

coefficient also shows a signature at the transition. Note that the latter is positive suggesting hole-like carriers in that portion of the phase diagram. The behaviour of the resistivity and sign of the Hall coefficient are consistent with recent experiments on Eu-227.^{11,12,15,17} Fig. 6 also shows the evolution of the resistivity as the ratio of the Hubbard repulsion to the bandwidth is reduced. The transition occurs at a lower temperature at $U = 0.9$ com-

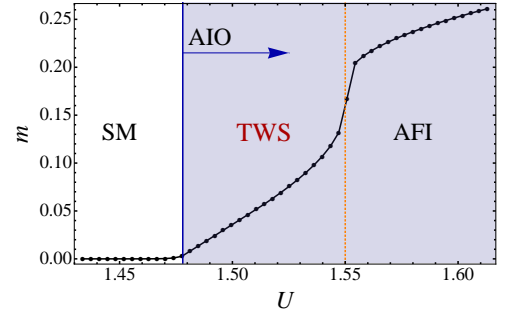


FIG. 4. Evolution of the magnetization, m , as a function of the Hubbard repulsion U for $t_\sigma = -0.775$. Note the abrupt evolution of m when going from the TWS to the AF insulator (AFI). The shaded regions have the AIO order.

pared to 1.25, as is expected because the onsite magnetization is reduced and the corresponding ground state has a smaller gap. At sufficiently small U , the system does not develop magnetic ordering and the $T = 0$ metallic bandstructure is present at all temperatures, in particular this leads to a finite $T = 0$ resistivity. This behaviour resembles what happens in the iridates as the size of the R-site ion is increased^{8,11,12} (chemical pressure). It also roughly agrees with hydrostatic pressure experiments on Eu-227¹⁷ with the difference that T_c was not found to change appreciably with pressure, unlike for Nd-227.¹⁸

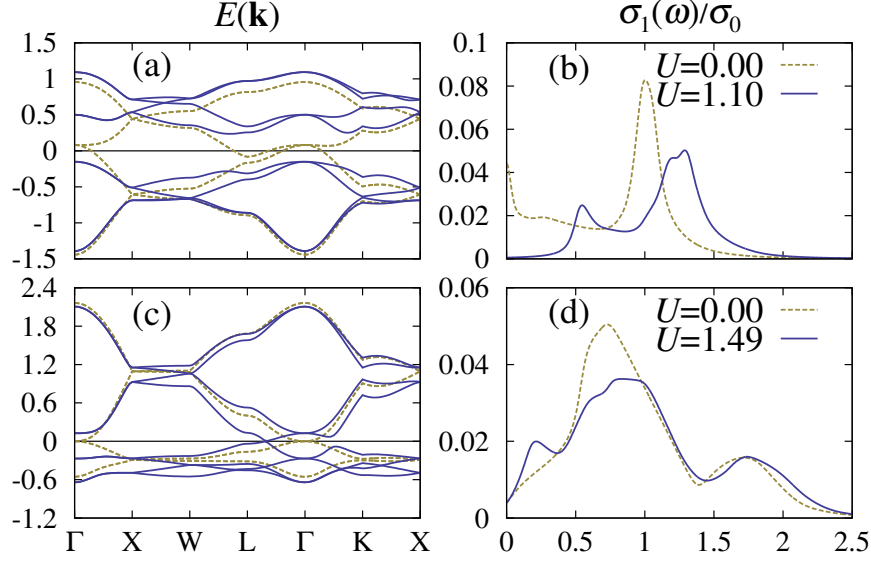


FIG. 5. Spectra and corresponding optical conductivity (real part) for $t_\sigma = -1.2$, a) & b), and $t_\sigma = -0.8$, c) & d), respectively. Panel a) shows the energy spectrum ($E_F = 0$) for the M and AIO insulator, while c) for the SM and TWS. The conductivity is in units of $\sigma_0 = e^2/\hbar a_0 \sim 10^4 (\Omega \cdot \text{cm})^{-1}$, where $a_0 = a/4$ and $a \approx 1.0$ nm is the FCC lattice constant.

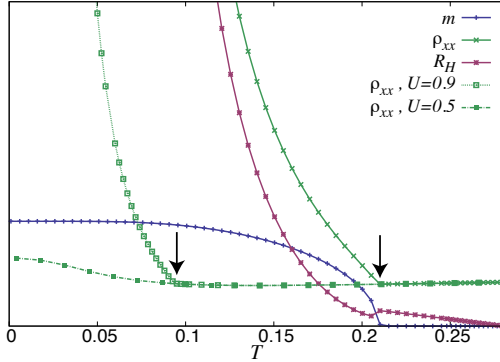


FIG. 6. Solid lines: on-site magnetization (m), DC resistivity (ρ_{xx}) and Hall coefficient (R_H) for $t_\sigma = -1.2$ and $U = 1.25$. The non-solid lines show ρ_{xx} for $U = 0.9$ and 0.5 . The arrows indicate the locations of the continuous transitions, at which ρ_{xx} shows a rapid upturn. The vertical axis goes from zero to positive values in arbitrary units.

V. MAGNETIC FIELD

We examine the effects of a magnetic field on some of the ground states of Fig. 2 via the addition of a Zeeman coupling to the Hubbard Hamiltonian. Since we ignore orbital coupling to the applied field, we focus on the non-metallic phases. We solve the self-consistent mean-field equations as above. We have considered fields along the [100], [110] and [111] directions. In all cases, we find a rather continuous evolution to a fully polarized paramagnetic state, without any first order transition to a FM aligned with the field, in contrast with claims made

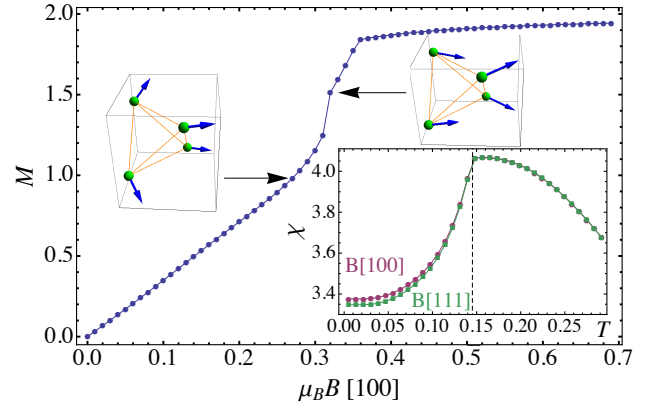


FIG. 7. Main: magnetization per unit cell, M , as a function of an applied magnetic field along the [100] direction for the AIO insulator at $t_\sigma = -1.2$ and $U = 2.1$. The evolution of the magnetic moments across an abrupt feature is shown. Inset: Susceptibility for fields along [100] and [111] versus T . The dashed line corresponds to the 2nd order transition.

in Ref. 5. Instead, the net magnetization grows until it (asymptotically) reaches a fully polarized state, as shown in Fig. 7 for the case of the AF insulator at $t_\sigma = -1.2$ and $U = 2.1$. The magnetization profiles generically present small features that correspond to sudden changes in the magnetic order (never to a FM, though), but lead to small changes in the actual magnetization. One such abrupt evolution is seen to occur around $\mu_B B \approx 0.32$ in Fig. 7. The magnetic susceptibility, χ , as a function of

temperature is shown in the inset of Fig. 7 for fields along [100] and [111]; with $\chi[110] = \chi[100]$. At temperatures above the magnetic melting transition, $T > T_c = 0.148$, χ is isotropic and slowly varying. As T is lowered, χ has a maximum at T_c , beyond which point it becomes slightly anisotropic. We find that in the ordered phase, $\chi[100] > \chi[111]$. All of these features are consistent with recent measurements of the zero-field cooled (ZFC) susceptibility of Eu-227.¹⁵

VI. DISCUSSION

We have introduced a microscopically-motivated Hamiltonian for the pyrochlore iridates, which contains all symmetry-allowed terms up to NNN. Its ground states include semimetals and metals, topological insulators, topological Weyl semimetals, gapped AF states with the all-in/all-out and related orders. Our phase diagram, Fig. 2, and results for the transport and magnetic properties at finite T and field suggest that our new model is apt to describe many salient features of the pyrochlore iridates family. In particular, in light of recent experiments^{11,15,17} that show the presence of a charge gap in Eu-227, we suggest that its ground state is an AIO gapped insulator, which under pressure can undergo a Lifshitz transition to a non-magnetic metal with small pockets, although TWS and metallic AF (with coexisting Weyl nodes and pockets) are possible. At sufficiently high temperatures, we find that the magnetic order melts continuously leading to a paramagnetic metal, consistent with experiments. For Y-227, which shows insulating behaviour at all temperatures ($d\rho/dT < 0$), we suggest that the high temperature non-magnetic state (connected to the $U = 0$ parent phase) is a semimetal. The TWS, which we find melts at relatively low temperatures, is probably not present in the ground states of Eu- and Y-227 because of the evidence for a finite gap but it might be accessible by hydrostatic pressure.^{17,18} Similarly, the ground state

of Nd-227 was suggested²⁰ to be poised near a metal-insulator transition (on the insulating side), potentially in the vicinity of the TWS.

In closing, we mention recent experiments on $\text{Bi}_2\text{Ir}_2\text{O}_7$ ^{31,32} which shows some similar properties to the other rare-earth based pyrochlore iridates. It was found that the resistivity of Bi-227 remains metallic down to sub-Kelvin temperatures,³¹ and recent μSR measurements³² have found evidence for a continuous transition into a long-range magnetically ordered state at ≈ 2 K. Moreover, the measurements suggest that the magnetic moments are very small. We observe that these features can be consistently fitted into our framework if we assume the ground state of Bi-227 is a metallic AF, see Fig. 2, which is obtained by “over-tilting” the TWS. Such a state carries the AIO order with small on-site moments. As a consequence, the continuous transition into a paramagnetic state occurs at a temperature much smaller than for the phases with a gapped AF ground state. An important caveat is that the Ir d -electrons will hybridize with the s - and p -orbitals of Bi,³¹ a feature that we do not take into account. Nevertheless, since our effective model is quite general, it may not be unreasonable to expect that it will capture some features of Bi-227.

ACKNOWLEDGEMENTS

We thank D. Drew and A. Sushkov for sharing preliminary optical conductivity data with us. We acknowledge helpful discussions with L. Balents, P. Baker, S. Bhattacharjee, S. R. Julian, A.J. Millis, S. Nakatsuji, J. Rau, and F. F. Tafti. This work was supported by NSERC, CIFAR, the Center for Quantum Materials at the University of Toronto (WWK,YBK), a Walter Sumner fellowship (WWK), and by the US Department of Energy under grant DOE FG02-04ER46169 (AG). Some part of this work was done at the Aspen Center for Physics, partially funded by NSF Grant #1066293.

Appendix A: Constructing the general Hamiltonian

We provide details regarding the construction of the Hamiltonian used in the main text. We choose the basis vectors of the pyrochlore lattice to be Fig. 8 a): $\mathbf{b}_1 = (0, 0, 0)$, $\mathbf{b}_2 = (0, 1, 1)$, $\mathbf{b}_3 = (1, 0, 1)$, $\mathbf{b}_4 = (1, 1, 0)$. In these units the FCC unit cell has dimension $a = 4$. As stated in the main text, the most general hopping Hamiltonian on the pyrochlore lattice takes the form:

$$H_0 = \sum_{\langle i,j \rangle} c_i^\dagger (t_1 + it_2 \mathbf{d}_{ij} \cdot \boldsymbol{\sigma}) c_j + \sum_{\langle\langle i,j \rangle\rangle} c_i^\dagger (t'_1 + i[t'_2 \mathcal{R}_{ij} + t'_3 \mathcal{D}_{ij}] \cdot \boldsymbol{\sigma}) c_j, \quad (\text{A1})$$

where the NN Hamiltonian is built using the vectors:

$$\mathbf{d}_{ij} = 2\mathbf{a}_{ij} \times \mathbf{b}_{ij}, \quad (\text{A2})$$

$$\mathbf{a}_{ij} = \frac{1}{2}(\mathbf{b}_i + \mathbf{b}_j) - \mathbf{x}_c, \quad (\text{A3})$$

$$\mathbf{b}_{ij} = \mathbf{b}_j - \mathbf{b}_i, \quad (\text{A4})$$

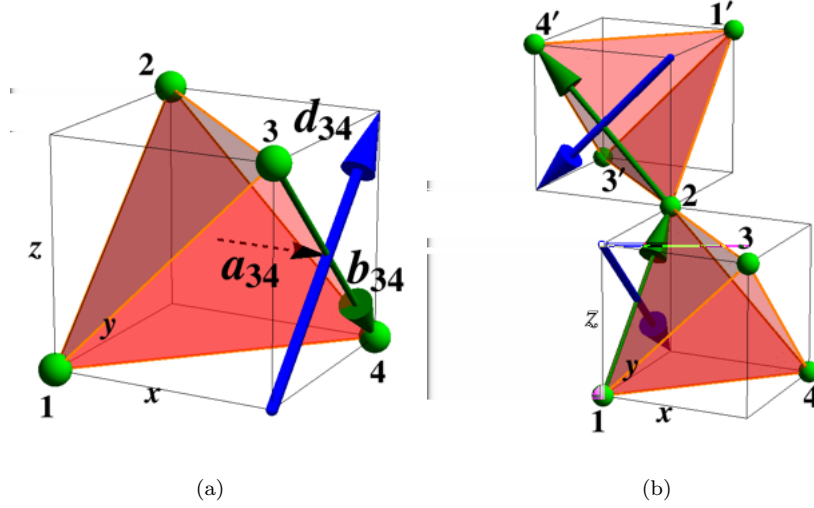


FIG. 8. Definitions of vectors entering into the general Hamiltonian. The green (thin) arrows correspond to the \mathbf{b}_{ij} , whereas the blue (thick) ones to the \mathbf{d}_{ij} . b) shows the vectors involved in obtaining the NNN hopping amplitude between sites 1 and 4', who share a common NN, site 2.

where it is understood in these definitions that \mathbf{b}_i selects the basis vector of the full lattice (Bravais + basis) index, i . \mathbf{a}_{ij} points from the center of the tetrahedron, $\mathbf{x}_c = (1, 1, 1)/2$, to the middle of the $\langle i, j \rangle$ bond; it is always orthogonal to the faces of the cube built out of the tetrahedron's vertices, see Fig. 8. \mathbf{b}_{ij} is the NN bond vector pointing from site i to site j . We have chosen the notation for the \mathbf{d}_{ij} in analogy with the Dzyaloshinski-Morya (DM) vectors, \mathbf{D}_{ij} , of a spin model on the pyrochlore lattice because both sets of vectors are parallel or antiparallel on all bonds. The difference arises in the sign. There are only two symmetry-allowed configurations of DM vectors,^{6,25} differing by a global sign. The \mathbf{d}_{ij} 's are always found to differ by a sign on some bonds with either type of DM vectors.

The NNN Hamiltonian simply uses cross products of the \mathbf{b}_{ij} 's and \mathbf{d}_{ij} 's:

$$\mathcal{R}_{ij} = \mathbf{b}_{ik} \times \mathbf{b}_{kj}, \quad (\text{A5})$$

$$\mathcal{D}_{ij} = \mathbf{d}_{ik} \times \mathbf{d}_{kj}, \quad (\text{A6})$$

where i and j are NNNs and share the site k as their (unique) common NN. $\mathcal{R}_{ij}, \mathcal{D}_{ij}$ are obtained by going to the NNN via the common NN site and taking a cross product of the two bond or \mathbf{d} vectors encountered, respectively. Fig. 8 b) illustrates the vectors necessary to construct the NNN amplitude between sites 1 and 4'. We note that \mathcal{R}_{ij} and \mathcal{D}_{ij} always point along the diagonals (s_1, s_2, s_3) , where $s_i = \pm 1$. For instance, $\mathcal{R}_{34} = (1, -1, 1)$ and $\mathcal{D}_{34} = (-1, 1, 1)$, as can be read off from Fig. 8; they are linearly independent as it should. For completeness, we provide the momentum-space form of the Hamiltonian, $H = \sum_{\mathbf{q}} c_a^\dagger(\mathbf{q})(\mathcal{H}_{ab}^{\text{NN}}(\mathbf{q}) + \mathcal{H}_{ab}^{\text{NNN}}(\mathbf{q}))c_b(\mathbf{q})$, with

$$\mathcal{H}_{ab}^{\text{NN}}(\mathbf{q}) = 2(t_1 + t_2 i\boldsymbol{\sigma} \cdot \mathbf{d}_{ab}) \cos[\mathbf{q} \cdot \mathbf{b}_{ab}], \quad (\text{A7})$$

$$\mathcal{H}_{ab}^{\text{NNN}}(\mathbf{q}) = 2 \sum_{c \neq a, b} \{t'_1(1 - \delta_{ab}) + i\boldsymbol{\sigma} \cdot [t'_2(\mathbf{b}_{ac} \times \mathbf{b}_{cb}) + t'_3(\mathbf{d}_{ac} \times \mathbf{d}_{cb})]\} \cos[\mathbf{q} \cdot (-\mathbf{b}_{ac} + \mathbf{b}_{cb})], \quad (\text{A8})$$

where the indices $1 \leq a, b, c \leq 4$ run over the basis sites. The sum over c in the NNN Hamiltonian runs over the choice of common NN between NNNs on sublattices a and b . There are two such sites: $c \in \{1, 2, 3, 4\} \setminus \{a, b\}$.

Ref. 27 discussed the t_1, t'_2 model, with a special focus on topological insulator phases. Ref. 28 identified the t_1, t_2 model as the most general NN, time-reversal-invariant hopping Hamiltonian on the pyrochlore lattice, for a single (pseudo)spin-1/2 Hilbert space per site. (We note that these two works use \mathbf{d}_{ij} to denote our \mathbf{b}_{ij} .)

1. Relation to microscopically motivated Hamiltonian

Two of us have previously proposed a model for the pyrochlore iridates, which was mainly analysed at the NN level.⁶ It extends a previous one² (although we focus on 2 spin/orbital degrees of freedom per site instead of 6) to which we added hopping amplitudes arising from the direct overlaps of the d-orbitals of Ir. These Slater-Koster like

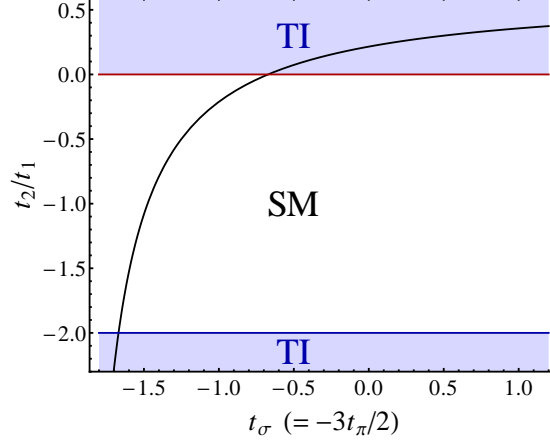


FIG. 9. The curve shows the relation between t_σ (in units of t_{oxy}) and t_2/t_1 , the latter coming from the general Hamiltonian Eq. (1).

models are more naturally constructed in a local basis because of the relative rotations between the oxygen octahedra within a unit cell, an illustration of this is found in Ref. 6. It is however useful to consider the same Hamiltonians expressed in a global basis instead, to see the role of the different microscopic hoppings more clearly.

We have taken the microscopic, local-axis Hamiltonian given by Eq. (1) in Ref. 6, supplemented by NNN direct hoppings, and have performed spinor rotations to obtain a Hamiltonian in a global basis for the pseudospin. This was compared with Eq. (A1) to obtain the relation between $\{t_1, t_2, t'_1, t'_2, t'_3\}$ and $\{t_{\text{oxy}}, t_\sigma, t_\pi, t'_\sigma, t'_\pi, t'_\delta\}$, as given in the main text. Compared with the main body, we in addition include the NNN hopping arising from the δ -overlap, t'_δ , leading to:

$$\begin{aligned} t_1 &= \frac{130t_{\text{oxy}}}{243} + \frac{17t_\sigma}{324} - \frac{79t_\pi}{243}; & t'_1 &= \frac{233t'_\sigma}{2916} - \frac{407t'_\pi}{2187} - \frac{1843t'_\delta}{8748}; \\ t_2 &= \frac{28t_{\text{oxy}}}{243} + \frac{15t_\sigma}{243} - \frac{40t_\pi}{243}; & t'_2 &= \frac{t'_\sigma}{1458} + \frac{220t'_\pi}{2187} + \frac{277t'_\delta}{4374}; \\ t'_3 &= \frac{25t'_\sigma}{1458} + \frac{460t'_\pi}{2187} - \frac{275t'_\delta}{4374}; \end{aligned} \quad (\text{A9})$$

The NNN hopping t'_δ was added in order to have a number of degrees of freedom matching that of the general Hamiltonian at the NNN level. One can also consider the NNN oxygen-mediated hopping, which will add an analogous term to the t'_i . Fig. 9 shows the relation between t_σ (in units of t_{oxy}) and t_2/t_1 , where we have set $t_\pi = -2t_\sigma/3$. The exact phase boundaries of the NN hopping Hamiltonian expressed using the Slater-Koster amplitudes can be obtained from the exact ones in the $t_1 - t_2$ model, $t_2/t_1 = -2, 0$: $t_\sigma = -192/115, -84/125 \approx -1.67, -0.67$, as can be verified in Fig. 9.

-
- ¹ B. J. Kim, H. Jin, S. J. Moon, J.-Y. Kim, B.-G. Park, C. S. Leem, J. Yu, T. W. Noh, C. Kim, S.-J. Oh, J.-H. Park, V. Durairaj, G. Cao, and E. Rotenberg, *Phys. Rev. Lett.* **101**, 076402 (2008); B. J. Kim, H. Ohsumi, T. Komesu, S. Sakai, T. Morita, H. Takagi, and T. Arima, *Science* **323**, 1329 (2009).
² D. Pesin and L. Balents, *Nat Phys* **6**, 376 (2010).
³ W. Witczak-Krempa, T. P. Choy, and Y. B. Kim, *Phys. Rev. B* **82**, 165122 (2010).
⁴ Y. Machida, S. Nakatsuji, S. Onoda, T. Tayama, and T. Sakakibara, *Nature* **463**, 210 (2009).
⁵ X. Wan, A. M. Turner, A. Vishwanath, and S. Y. Savrasov, *Phys. Rev. B* **83**, 205101 (2011).
⁶ W. Witczak-Krempa and Y. B. Kim, *Phys. Rev. B* **85**, 045124 (2012).
⁷ A. Go, W. Witczak-Krempa, G. S. Jeon, K. Park, and Y. B. Kim, *Phys. Rev. Lett.* **109**, 066401 (2012).
⁸ D. Yanagishima and Y. Maeno, *Journal of the Physical Society of Japan* **70**, 2880 (2001).
⁹ N. Taira, M. Wakeshima, and Y. Hinatsu, *Journal of Physics: Condensed Matter* **13**, 5527+ (2001).
¹⁰ H. Fukazawa and Y. Maeno, *Journal of the Physical Society of Japan* **71**, 2578 (2002).

- ¹¹ K. Matsuhira, M. Wakeshima, R. Nakanishi, T. Yamada, A. Nakamura, W. Kawano, S. Takagi, and Y. Hinatsu, *Journal of the Physical Society of Japan* **76**, 043706+ (2007).
- ¹² K. Matsuhira, M. Wakeshima, Y. Hinatsu, and S. Takagi, *Journal of the Physical Society of Japan* **80**, 094701 (2011).
- ¹³ T. Hasegawa, N. Ogita, K. Matsuhira, S. Takagi, M. Wakeshima, Y. Hinatsu, and M. Udagawa, *Journal of Physics: Conference Series* **200**, 012054+ (2010).
- ¹⁴ S. Zhao, J. M. Mackie, D. E. MacLaughlin, O. O. Bernal, J. J. Ishikawa, Y. Ohta, and S. Nakatsuji, *Phys. Rev. B* **83**, 180402 (2011).
- ¹⁵ J. J. Ishikawa, E. C. T. O'Farrell, and S. Nakatsuji, *Phys. Rev. B* **85**, 245109 (2012).
- ¹⁶ K. Tomiyasu, K. Matsuhira, K. Iwasa, M. Watahiki, S. Takagi, M. Wakeshima, Y. Hinatsu, M. Yokoyama, K. Ohoyama, and K. Yamada, *Journal of the Physical Society of Japan* **81**, 034709+ (2012).
- ¹⁷ F. F. Tafti, J. J. Ishikawa, A. McCollam, S. Nakatsuji, and S. R. Julian, *Phys. Rev. B* **85**, 205104 (2012).
- ¹⁸ M. Sakata, T. Kagayama, K. Shimizu, K. Matsuhira, S. Takagi, M. Wakeshima, and Y. Hinatsu, *Phys. Rev. B* **83**, 041102 (2011).
- ¹⁹ M. C. Shapiro, S. C. Riggs, M. B. Stone, C. R. de la Cruz, S. Chi, A. A. Podlesnyak, and I. R. Fisher, *Phys. Rev. B* **85**, 214434 (2012).
- ²⁰ S. M. Disseler, C. Dhital, T. C. Hogan, A. Amato, S. R. Giblin, C. de la Cruz, A. Daoud-Aladine, S. D. Wilson, and M. J. Graf, *Phys. Rev. B* **85**, 174441 (2012).
- ²¹ S. M. Disseler, C. Dhital, A. Amato, S. R. Giblin, C. de la Cruz, S. D. Wilson, and M. J. Graf, *Phys. Rev. B* **86**, 014428 (2012).
- ²² G. Chen and M. Hermele, *Phys. Rev. B* **86**, 235129 (2012).
- ²³ B.-J. Yang and Y. B. Kim, *Phys. Rev. B* **82**, 085111 (2010).
- ²⁴ M. Kargarian, J. Wen, and G. A. Fiete, *Phys. Rev. B* **83**, 165112 (2011).
- ²⁵ M. Elhajal, B. Canals, R. Sunyer, and C. Lacroix, *Phys. Rev. B* **71**, 094420 (2005).
- ²⁶ J. E. Moore and L. Balents, *Phys. Rev. B* **75**, 121306 (2007); R. Roy, *Phys. Rev. B* **79**, 195322 (2009); L. Fu, C. L. Kane, and E. J. Mele, *Phys. Rev. Lett.* **98**, 106803 (2007).
- ²⁷ H.-M. Guo and M. Franz, *Phys. Rev. Lett.* **103**, 206805 (2009).
- ²⁸ M. Kurita, Y. Yamaji, and M. Imada, *Journal of the Physical Society of Japan* **80**, 044708+ (2011).
- ²⁹ N. P. Ong, *Phys. Rev. B* **43**, 193 (1991).
- ³⁰ D. Podolsky and Y. B. Kim, *Phys. Rev. B* **83**, 054401 (2011).
- ³¹ T. F. Qi, O. B. Korneta, X. Wan, L. E. DeLong, P. Schlottmann, and G. Cao, *Journal of Physics: Condensed Matter* **24**, 345601 (2012).
- ³² P. J. Baker, J. S. Moeller, F. L. Pratt, W. Hayes, S. J. Blundell, T. Lancaster, T. F. Qi, and G. Cao, ArXiv e-prints (2013), [arXiv:1302.6905 \[cond-mat.str-el\]](https://arxiv.org/abs/1302.6905).